A single-phase, non-isothermal model for PEM fuel cells

Hyunchul Ju, Hua Meng, Chao-Yang Wang *

Department of Mechanical and Nuclear Engineering, Electrochemical Engine Center (ECEC), The Pennsylvania State University, University Park, PA 16802, USA

Abstract

A proton exchange membrane (PEM) fuel cell produces a similar amount of waste heat to its electric power output, and tolerates a small temperature deviation from its design point for best performance and durability. These stringent thermal requirements present a significant heat transfer problem. In this work, a three-dimensional, non-isothermal model is developed to account rigorously for various heat generation mechanisms, including irreversible heat due to electrochemical reactions, entropic heat, and Joule heating arising from the electrolyte ionic resistance. The thermal model is further coupled with the electrochemical and mass transport models, thus permitting a comprehensive study of thermal and water management in PEM fuel cells. Numerical simulations reveal that the thermal effect on PEM fuel cells becomes more critical at higher current density and/or lower gas diffusion layer thermal conductivity. This three-dimensional model for single cells forms a theoretical foundation for thermal analysis of multi-cell stacks where thermal management and stack cooling is a significant engineering challenge.
© 2004 Elsevier Ltd. All rights reserved.

1. Introduction

A proton exchange membrane fuel cell (PEMFC) produces nearly a similar amount of waste heat to its electric power output so as to render its energy-conversion efficiency of roughly 50%. For an automotive fuel cell engine rated at 100 kW, this means 100 kW heat dissipation rate. Moreover, PEM fuel cells tolerate a small temperature variation because the membrane proton conductivity strongly depends on the degree of its hydration and hence on the membrane temperature as the vapor saturation pressure is an exponent function of temperature. Also, formation of a hot spot locally could

severely deteriorate the membrane durability. For these reasons, thermal management in a PEM fuel cell is inherently coupled with water management, and the two factors combine to ensure high performance and durability of a PEM fuel cell. It is thus of paramount importance to understand the thermal behavior under various design and operating conditions and furthermore develop a capability to accurately predict the temperature distribution in PEM fuel cells.

Thermal modeling of a PEM fuel cell starts with the energy equation that balances heat generation from the cell with heat removal from it. Heat generation in a fuel cell undergoing no phase change includes entropic heat of reactions, the irreversible heat of electrochemical reactions, and Joule heating [1]. Roughly, the irreversible reaction heat, entropic heat and Joule heating in a PEMFC account for 55%, 35% and 10% of total heat release, respectively. The entropic heat, also called

* Corresponding author. Tel.: +1 814 863 4762; fax: +1 814 863 4848.

E-mail address: cxw31@psu.edu (C.-Y. Wang).

Nomenclature

a	water activity
A	area, m^2
c	molar concentration, mol/m^3
cgc	cathode gas channel
D	mass diffusivity of species, m^2/s
EW	equivalent molecular weight of electrolyte in membrane, kg/mol
F	Faraday constant, $96487\,C/mole$
I	current density, A/m^2
j	transfer current, A/m^3
k	thermal conductivity, $W/m\,K$
K	hydraulic permeability, m^2
p	pressure, Pa
mc	membrane facing with gas channels
mr	membrane facing with current collector ribs
n	number of electrons in electrochemical reaction
n_d	electro-osmotic drag coefficient
R	the universal gas constant, $8.314\,J/mol\,K$
RH	relative humidity
s	stoichiometry coefficient in electrochemical reaction
S	source term in transport equation
T	temperature, K
$\mathbf{u}$	velocity vector, m/s
V_{cell}	cell potential, V
U_0	thermodynamic equilibrium potential, V

Greek symbols

α	transfer coefficient
ε	volume fraction of gaseous phase in porous region
ε_{mc}	volume fraction of ionomer phase in catalyst layer
ϕ	phase potential, V
η	overpotential, V
η_e	energy efficiency
κ	ionic conductivity, S/m
λ	membrane water content, mol H_2O/mol SO_3^-
μ	fluid viscosity, kg/m s

ρ	density, kg/m^3
$\rho_{dry,mem}$	dry membrane density, kg/m^3
τ	viscous stress, N/m^2
ζ	stoichiometry flow ratio

Subscripts

a	anode
avg	average value
c	cathode
cat	catalyst
e	electrolyte
g	gas phase
GDL	gas diffusion layer
H_2	hydrogen
i	regions index
irrev	irreversible reaction heat
in	channel inlet
jouleH	joule heating
mem	membrane
k	species index
O_2	oxygen
react	electrochemical reaction
ref	reference value
rev	reversible reaction heat(entropic heat)
sat	saturation value
T	energy equation
u	momentum equation
w	water
Φ	potential equation
0	standard condition, 298.15 K and 101.3 kPa (1 atm)

Superscripts

e	electrolyte
eff	effective value in porous region
mem	membrane
g	gas
ref	reference value
sat	saturation value

reversible heat or Peltier effect [1], is the difference between the total chemical energy of reactants and the maximum usable work according to the second law of thermodynamics. The irreversible heat results from the irreversibility of the electrochemical reactions, and the Joule heating is caused by finite resistances of various components used in PEMFC.

A number of thermal PEMFC models have appeared in the literature. Early efforts were made by Nguyen and White [2] and Fuller and Newman [3]. Nguyen and White [2] developed a two-dimensional PEMFC model with one-dimensional heat transfer in the flow direction. The model considers phase change of water in the flow channel as the only heat source, allowing convective heat transfer between gas and solid phases. On the other hand, Fuller and Newman [3] developed a pseudo two-dimensional thermal PEMFC model with one-dimensional mass transfer in the through-membrane direction and one-dimensional heat transfer in the flow direction. Based on the known enthalpy change of the overall elec-

trochemical reactions, the model calculated the temperature rise of the flowing gas streams with various external heat transfer coefficients. However in these early models, the temperature of membrane and electrodes were not differentiated, despite that a significant temperature variation in those regions exists in both the through-membrane and flow directions depending on the geometric and operating conditions. Furthermore, the major heat source terms, the entropic and irreversible reaction heats, were not specified in their models. Yi and Nguyen [4] extended Nguyen and White's model to include the entropic and irreversible reaction heats along with the phase change heat. However, this model allowed the temperature variation of the solid phase in the flow direction only, assuming uniform temperature in the through-membrane direction.

Wöhr et al. [5] developed a one-dimensional thermal model for heat and mass transfer in the through-membrane direction, particularly for PEMFC stacks. Accounting for the entropic and irreversible reaction heats, they computed the temperature profile in the through-membrane direction and predicted the maximum temperature as a function of the number of cells contained in a stack. Rowe and Li [6] also developed a one-dimensional model in the through-membrane direction. Including entropic, irreversible, and phase change heats, they further took account of Joule heating in the membrane and anode/cathode catalyst layers. This work predicted the temperature variation in the through-membrane direction under the various current densities and electrode thermal conductivities. The major drawback of this model is that the cathode catalyst layer is assumed to be fully hydrated and the membrane water content is linearly interpolated, indicating a lack of accuracy of the model in low humidity operation.

Multi-dimensional thermal models were presented by many PEMFC modeling groups. Maggio et al. [7] performed pseudo three-dimensional simulations, neglecting the temperature gradient in the flow direction. However, they only considered the overall heat source term as $(U_0 - V_{cell})I$. In the three-dimensional models developed by Shimpalee and Dutta [8] and Costamagna [9], the heat source terms were also treated globally and not made location-specific. Berning et al. [10] presented a three-dimensional PEMFC model including irreversible and entropic heat terms in the catalyst layers and Joule heating in the membrane. The main drawback of this model is to assume the membrane to be fully humidified, indicating limited applicability to low-humidity operating conditions. Zhou and Liu [11] developed a three-dimensional PEMFC model in which the entropic reaction heat (~35% of total heat) was neglected.

As indicated above, the reversible reaction heat, $I(-T\frac{\partial U_0}{\partial T})$, was often overlooked in the majority of thermal modeling work in the literature. However it is a significant contributor to overall heat generation (>30% of

total heat release). In addition, unambiguous and location-specific heat generation expressions must be developed for use in detailed multi-dimensional PEMFC models that include gas channels, gas diffusion layers, catalyst layers, and membrane. In this paper, we present a rigorous model to describe the coupled electrochemical and thermal phenomena occurring in PEM fuel cells, with focus on the correct expressions of various heat generation sources. Subsequently, we carry out three-dimensional numerical simulation and particularly present an analysis of overall energy balance on three-dimensional numerical results to elucidate the relative importance of each heat generation mechanism. Finally, we perform a numerical parametric study to investigate the impact of cell voltage, GDL thermal conductivity, and feed gas relative humidity on electrochemical and thermal behaviors of PEMFC.

2. Physical and numerical model

2.1. Thermodynamic calculation of total heat generation

The total heat release from a PEM fuel cell can be readily derived according to thermodynamics. Consider a H_2/O_2 fuel cell operated at the temperature, T, pressure, P, and the current density, I on the electrode surface area, A_{react}. The reversible heat release, Q_{rev}, can be written as:

$$Q_{rev} = (-T\Delta S) \cdot \dot{n}_{H_2} = (-T\Delta S) \cdot \frac{I}{2F} \cdot A_{react}$$
$$= \left(-T\frac{\partial U_0}{\partial T}\right) \cdot I \cdot A_{react} \qquad (1)$$

where ΔS represents the entropy change of the overall reaction, $H_2 + \frac{O_2}{2} \rightarrow H_2O$, and U_0 the thermodynamic equilibrium potential of the reaction [12]. In addition, there exists irreversible heat generation due to the cell operated at a different voltage, V_{cell}, from the equilibrium, U_0. This additional heat generate rate is simply given by:

$$Q_{irrev} = \left(-\frac{\Delta G}{2F} - V_{cell}\right) \cdot I \cdot A_{react}$$
$$= (U_0 - V_{cell}) \cdot I \cdot A_{react} \qquad (2)$$

where ΔG is the free energy change of the H_2/O_2 reaction. This irreversible heat generation is attributed to ohmic and activation polarizations in a PEMFC. The total heat generation, Q_{total}, is thus given by:

$$Q_{total} = Q_{rev} + Q_{irrev}$$
$$= \left(-T\frac{\partial U_0}{\partial T}\right) \cdot I \cdot A_{react} + (U_0 - V_{cell}) \cdot I \cdot A_{react}$$
$$= \left(U_0 - T\frac{\partial U_0}{\partial T}\right) \cdot I \cdot A_{react} - V_{cell} \cdot I \cdot A_{react} \qquad (3)$$

Notice that the first term on the right side of Eq. (3) is the maximum chemical power available from the overall reaction and the second term is the actual electrical power produced by a fuel cell. The energy efficiency can then be conveniently defined as the ratio of these two terms.

$$\eta_e = \frac{V_{cell} \cdot I \cdot A_{react}}{\left(U_0 - T\frac{\partial U_0}{\partial T}\right) \cdot I \cdot A_{react}} = \frac{V_{cell}}{U_0 - T\frac{\partial U_0}{\partial T}} \tag{4}$$

2.2. Multi-dimensional governing equations and their assumptions

The present three-dimensional, non-isothermal, electrochemical-transport coupled model is developed based on the previous work of Um et al. [13] and Gu and Wang [14]. The thermal PEMFC model considers all seven sub-regions of a PEMFC: gas channels, diffusion and catalyst layers on both anode and cathode sides, and the ionomeric membrane.

The assumptions made in the present model are as follows: (1) ideal gas mixtures; (2) isotropic and homogeneous electrode, catalyst layers and membrane; (3) incompressible and laminar flow due to small pressure gradients and flow velocities; (4) negligible ohmic potential drop in the electronically-conductive solid matrix of porous electrodes and catalyst layers, as well as in the current collectors due to their relatively very large electric conductivities; and (5) the single-phase assumption for water transport.

Due to Assumption (4), the electrode becomes an equi-potential line such that

$$\phi_s = 0 \quad \text{for anode}$$

$$\phi_s = V_{cell} \quad \text{for cathode}$$

Assumption (4) also implies that ohmic Joule heating in the current collectors, GDL and catalyst layers is negligible due to their high electric conductivities. Assumption (5) implies that water can exist in super-saturation in the gas phase, thus being similar to the treatment of Springer et al. [15], where the water activity is allowed to be greater than unity. The heat release/absorption due to phase change of water is also excluded in lieu of Assumption (5).

Under these assumptions, the PEMFC thermal model consists of conservation equations of mass, momentum, chemical species, electric charge and thermal energy. A single-domain approach is used to make a single set of governing equations valid for all sub-regions. So no interfacial conditions are required to specify at internal boundaries between various regions. All the governing equations are summarized in Table 1 with their respective volumetric source terms identified for various sub-regions of a fuel cell. Brief comments on each of the five governing equations follow.

In porous regions, superficial velocities are used in order to automatically ensure mass flux continuity at the interface between porous and non-porous regions. Also notice that intrinsic transport properties in the porous regions are modified into effective transport properties to account for the effects of porosity and tortuosity via the Bruggeman correlation [16]. The source terms in the momentum equations are devised to recover Darcy's law under the limiting condition where the permeability of the porous medium is small and hence the velocity is small.

The source term in the charge equation is used to describe the transfer current between the solid matrix and the electrolyte phase inside each of anode and cathode catalysts layers. The transfer current densities are expressed as follows:

$$\text{Anode}: \quad j = ai_{0,a}^{ref}\left(\frac{C_{H_2}}{C_{H_2,ref}}\right)^{1/2}\left(\frac{\alpha_a + \alpha_c}{RT} \cdot F \cdot \eta\right) \tag{12}$$

$$\text{Cathode}: \quad j = -ai_{0,c}^{ref}\left(\frac{C_{O_2}}{C_{O_2,ref}}\right)\exp\left(-\frac{\alpha_c}{RT} \cdot F \cdot \eta\right) \tag{13}$$

These kinetic expressions represent the hydrogen oxidation reaction (HOR) in the anode catalyst layer and oxygen reduction reaction (ORR) in the cathode catalyst layer, respectively. These are simplified from the general Butler–Volmer equation. The HOR kinetic expression is derived by linearizing the Butler–Volmer equation on the assumption that the HOR reaction is facile and hence the surface overpotential is small. On the other hand, the ORR kinetic reaction is slow, causing high overpotential. Therefore the ORR kinetic expression is obtained by neglecting the anodic reaction term of the Butler–Volmer equation. The value of $(\alpha_a + \alpha_c)$ in HOR kinetics should be equal to 2, while $\alpha_c = 1$ in ORR corresponds to a Tafel slope of approximately 60 mV/decade. It should be noted that the ORR is assumed to be the first order reaction based on early experimental work of Bernardi and Verbrugge [17] and Gottesfeld and Zawodzinski [18]. By assuming the reference open-circuit potentials of anode and cathode to be zero and a function of temperature, respectively, the expressions of surface overpotential for anode and cathode sides can be defined, respectively, as:

$$U_0 = \phi_s - \phi_e - U_0 \tag{14}$$

where the thermodynamic equilibrium potential, U_0, is given by

$$U_0 = 0 \qquad \text{for anode}$$
$$U_0 = 1.23 - 9.0 \times 10^{-4}(T - 298.15) \quad \text{for cathode} \tag{15}$$

This equilibrium potential for a H_2/air fuel cell is calculated from thermodynamic data of reaction enthalpy and entropy changes. Based on the experimental data given by Parthasarathy et al. [19], the temperature

Table 1
Single-phase non-isothermal PEMFC model: governing equations with source terms

	Conservation equations		Source terms
Mass	$\nabla \cdot (\rho \vec{u}) = 0$	(5)	
Momentum	$\dfrac{1}{\varepsilon^2} \nabla \cdot (\rho \vec{u}\vec{u}) = -\nabla p + \nabla \cdot \tau + S_u$	(6)	In diffusion and catalyst layers: $S_u = -\dfrac{\mu}{K}\vec{u}$
Species	$\nabla \cdot (\vec{u}C_k) = \nabla \cdot (D_k^{\mathrm{eff}} \nabla C_k) + S_k$	(7)	In catalyst layers: $S_k = -\dfrac{s_k j}{nF}$
			For water in catalyst layers: $S_k = -\nabla \cdot \left(\dfrac{n_{\mathrm{d}}}{F}I\right) - \dfrac{s_k j}{nF}$
Charge	$\nabla \cdot (\kappa^{\mathrm{eff}} \nabla \Phi_{\mathrm{e}}) + S_\Phi = 0$	(8)	In catalyst layers: $S_\Phi = j$
Energy	$\nabla \cdot (\rho C_{\mathrm{P}} \vec{u}T) = \nabla \cdot (k^{\mathrm{eff}} \nabla T) + S_T$	(9)	In catalyst layers: $S_T = j\left(\eta + T\dfrac{\mathrm{d}U_0}{\mathrm{d}T}\right) + \dfrac{I^2}{\kappa^{\mathrm{eff}}}$
			In membrane: $S_T = \dfrac{I^2}{\kappa^{\mathrm{eff}}}$

Electrochemical reaction: $\sum_k s_k M_k^z = ne^-$, where $\begin{cases} M_k \equiv \text{chemical formula of species } k \\ s_k \equiv \text{stoichiometry coefficient} \\ n \equiv \text{number of electrons transferred} \end{cases}$

Hydrogen oxidation reaction (HOR) in anode side:

$$H_2 - 2H^+ = 2e^- \tag{10}$$

Oxygen reduction reaction (ORR) in cathode side:

$$2H_2O - O_2 - 4H^+ = 4e^- \tag{11}$$

dependence of the ORR kinetic parameter is approximated as follows:

$$ai_{0,c}^{\mathrm{ref}}(T) = ai_{0,c}^{\mathrm{ref}}(353\,\mathrm{K}) \cdot \exp\left[-16456\left(\frac{1}{T} - \frac{1}{353.15}\right)\right] \tag{16}$$

The source terms in the species equations represent the production or consumption of species k by the electrochemical reactions (i.e. anode HOR and cathode ORR) and the electro-osmotic drag of water from the anode to cathode. The mass diffusion coefficient of species k, D_k, in the anode and cathode gas channels is calculated as a function of temperature and pressure [20]. For the porous regions of a PEM fuel cell such as the gas diffusion and catalyst layers, the expression is modified into the effective species diffusivity, D_k^{eff} using Bruggman correlation [16].

$$D_k = D_0\left(\frac{T}{T_0}\right)^{3/2}\left(\frac{P_0}{P}\right) \quad \text{for gas channels} \tag{17}$$

$$D_k^{\mathrm{eff}} = \varepsilon_i^{1.5} \cdot D_k \quad \text{for porous regions} \tag{18}$$

The three heat source terms in the energy equation deserve special attention. They represent irreversible heat of the electrochemical reaction, reversible entropic heat, and Joule heating, respectively. Gu and Wang [14] provided the location-specific expressions for these terms as shown in Table 1. In addition, the effective heat capacitance in a porous material consisting of the matrix and fluid is given by

$$\rho C_{\mathrm{P}} = \varepsilon(\rho C_{\mathrm{P}})_{\mathrm{f}} + (1 - \varepsilon) \cdot (\rho C_{\mathrm{P}})_{\mathrm{s}} \tag{19}$$

where the heat capacitances (ρC_{P}) with subscripts "f" and "s" are referred to as the fluid and the solid matrix, respectively.

Transport properties of the electrolyte are given by Springer et al. [15] for Nafion membranes. The proton conductivity, κ_{mem}, and the electro-osmotic drag coefficient for water, n_{d}, in the membrane are correlated with the water content of the membrane, λ, which is in turn a function of the water activity, a.

$$a = \frac{C_{\mathrm{w}}^{\mathrm{g}} RT}{P^{\mathrm{sat}}} \tag{20}$$

$$\lambda = \begin{cases} 0.043 + 17.81a - 39.85a^2 + 36.0a^3 & \text{for } 0 < a \leqslant 1 \\ 14 + 1.4(a - 1) & \text{for } 1 < a \leqslant 3 \end{cases} \tag{21}$$

$$\kappa_{\text{mem}} = (0.5139\lambda - 0.326)\exp\left[1268\left(\frac{1}{303} - \frac{1}{T}\right)\right] \quad (22)$$

$$n_{\text{d}} = \frac{2.5\lambda}{22} \quad (23)$$

The mass diffusivity of species k through the membrane is usually much lower than that in gas. The diffusivities of H_2 and O_2 in the membrane are taken to be constant and their values listed in Table 2. The water diffusivity in the membrane follows that of Motupally et al. [21]:

$$D_{\text{w,mem}} = \begin{cases} 3.1 \times 10^{-7}\lambda(e^{0.28\lambda} - 1) \cdot e^{(-2346/T)} \\ \quad \text{for } 0 < \lambda \leqslant 3 \\ 4.17 \times 10^{-8}\lambda(1 + 161e^{-\lambda}) \cdot e^{(-2346/T)} \\ \quad \text{otherwise} \end{cases} \quad (24)$$

The equivalent water concentration in the membrane is defined as

$$C_{\text{w,mem}} = \frac{\rho_{\text{dry,mem}}\lambda}{EW} \quad (25)$$

In the present work, we choose Gore-Select® membrane as the electrolyte for parametric studies due to its popular application in the industry. Gore membrane is a microscopically reinforced composite membrane and has only about half of the proton conductivity and water diffusivity of the Nafion membrane. Hence, it follows that

$$\begin{aligned}\kappa_{\text{mem}}^{\text{eff}} &= \frac{1}{2} \cdot \kappa_{\text{mem}} \\ &= \frac{1}{2} \cdot (0.5139\lambda - 0.326)\exp\left[1268\left(\frac{1}{303} - \frac{1}{T}\right)\right]\end{aligned} \quad (26)$$

$$D_{\text{w,mem}}^{\text{eff}} = \frac{1}{2}D_{\text{w,mem}} \quad (27)$$

However, Nafion solution is still used as the ionomer in the anode and cathode catalyst layers. Consequently, the effective proton conductivity of the anode and cathode catalyst layers follows that of Nafion membrane but with the Bruggmann correlation [16]. That is,

$$\kappa_{\text{cat}}^{\text{eff}} = \varepsilon_{\text{mc}}^{1.5} \cdot \kappa_{\text{mem}} \quad (28)$$

where ε_{mc} is the volume fraction of ionomer in the anode and cathode catalyst layers.

Once the electrolyte phase potential, ϕ_{e} and the proton conductivity on the membrane, $\kappa_{\text{mem}}^{\text{eff}}$ are obtained, local current density, I, can be calculated by:

$$I = -\kappa_{\text{mem}}^{\text{eff}}\nabla\phi_{\text{e}} \quad (29)$$

The average current density can then be obtained by taking the surface average of the local current density over the entire membrane. That is,

$$I_{\text{avg}} = \frac{1}{A_{\text{mem}}}\int_{A_{\text{mem}}} I\,\text{d}A \quad (30)$$

Table 2
Physical parameters and properties

Description	Value
Anode/cathode gas channel width	3.180 mm
Anode/cathode gas diffusion layers width	0.235 mm
Anode/cathode catalyst layers width	0.010 mm
Membrane width (Gore-select®)	0.018 mm
Effective porosity of anode/cathode gas diffusion layers, $\varepsilon_{\text{GDL}}^{\text{eff}}$	0.6
Effective porosity of anode/cathode catalyst layers, $\varepsilon_{\text{cat}}^{\text{eff}}$	0.6
Volume fraction of ionomer in anode/cathode catalyst layers, ε_{mc}	0.26
Permeability of anode/cathode gas diffusion layers, K	2.0×10^{-12} m²
Exchange current density × ratio of reaction surface to catalyst layer volume in anode side, $ai_{0,\text{a}}^{\text{ref}}$	1.0×10^{9} A/m³
Exchange current density × ratio of reaction surface to catalyst layer volume in cathode side, $ai_{0,\text{c}}^{\text{ref}}$	3.0×10^{3} A/m³
Reference hydrogen molar concentration, $c_{H_2,\text{ref}}$	40.88 mol/m³
Reference oxygen molar concentration, $c_{O_2,\text{ref}}$	40.88 mol/m³
Anodic and cathodic transfer coefficients for hydrogen oxidation reaction	$\alpha_{\text{a}} = \alpha_{\text{c}} = 1$
Cathodic transfer coefficient for oxygen reduction reaction	$\alpha_{\text{c}} = 1$
Dry membrane density, $\rho_{\text{dry,mem}}$	2000 kg/m³
Equivalent weight of electrolyte in membrane, EW	1.1 kg/mol
Faraday Constant, F	96487 C/mol
Universal gas constant, R	8.314 J/mol K
H_2 diffusivity in membrane, $D_{H_2}^{\text{e}}$	2.59×10^{-10} m²/s
O_2 diffusivity in membrane, $D_{O_2}^{\text{e}}$	1.22×10^{-10} m²/s
H_2 diffusivity in the anode gas channel, $D_{0,H_2,\text{a}}$	1.1028×10^{-4} m²/s
H_2O diffusivity in the anode gas channel, $D_{0,\text{w,a}}$	1.1028×10^{-4} m²/s
O_2 diffusivity in the cathode gas channel, $D_{0,O_2,\text{c}}$	3.2348×10^{-5} m²/s
H_2O diffusivity in the cathode gas channel, $D_{0,\text{w,c}}$	7.35×10^{-5} m²/s

2.3. Boundary conditions

Eqs. (5)–(9) in Table 1 form a complete set of governing equations for seven unknowns: $\vec{u}$, p, T, C_{H_2}, C_{O_2}, C_w, and ϕ_e. By use of the single-domain approach, the boundary conditions are required only at the external surfaces of the computational domain. The no-flux condition is applied to the external surfaces except for the inlets and outlets of the anode/cathode gas channels. At the anode/cathode inlet, the inlet species concentrations, $c_{k,in}$, are determined by the inlet pressure and humidity conditions. The anode/cathode inlet velocities can be calculated by their respective stoichiometric flow ratios, ζ_a and ζ_c, which are defined as the ratio of the amount of reactant supplied to the amount of reactant required by the electrochemical reaction to generate the specified reference current density, I_{ref}:

$$V_{a,in} = \zeta_a \cdot \frac{I_{ref}}{2F \cdot C_{H_2,in}} \cdot \frac{A_{react}}{A_{a,in}} \tag{31}$$

$$V_{c,in} = \zeta_c \cdot \frac{I_{ref}}{4F \cdot C_{O_2,in}} \cdot \frac{A_{react}}{A_{c,in}} \tag{32}$$

The outlet species and velocity conditions are the fully-developed ones, i.e. the gradient of each variable is zero. For thermal boundary conditions, a constant temperature is applied to the anode and cathode gas inlets as well as the anode and cathode flow plate surfaces.

2.4. Numerical implementation

The PEMFC model described above is implemented into a commercial computational fluid dynamics (CFD) package, STAR-CD, basing on its user-coding capability [22]. All source terms in Table 1 are specified through the user code. Fig. 1 display the schematic diagram of a single-channel fuel cell to be solved in this study. Based on the grid-independence study of Meng and Wang [23], the number of grid points used in the present model are 56 in the through-membrane direction and 112 in the flow direction. In the in-plane direction,

Fig. 1. Mesh configuration of the numerical PEMFC model with a single flow channel.

defined to be across the channel through the rib area, 10 and 5 grid points are respectively used for the channel and current collector ribs. As a result, roughly 140,000 computational cells are used to simulate the single-channel fuel cell. The computational time required for the present 3D non-isothermal simulation is roughly 3–4 h on a single PC (2 GHz).

3. Results and discussion

There are two principal effects of the increased temperature in the membrane-electrode assembly (MEA) on cell performance. One is the enhanced ORR kinetics at higher temperatures (see Eq. (16)), which improves the fuel cell performance. However, the increase in the membrane temperature also results in much higher saturation pressure and thus may lower water activity and proton conductivity of the membrane. The adverse effect of increasing temperature on the membrane ionic resistance must be then balanced with the beneficial effect on ORR kinetics, demonstrating a need for coupled thermal and water management in a PEM fuel cell. In this section, we shall use 3D numerical results to illustrate these two conflicting effects of the temperature.

We assess the effects of three critical parameters that are expected to dominate the thermal behavior of a PEM fuel cell. The first one is the thermal conductivity of the gas diffusion layer (GDL), which is a few orders of magnitude higher than those of the gas mixtures. Heat generated in the catalyst layer is primarily removed through the GDL to the current collector rib by lateral conduction. This process is controlled by the GDL thermal conductivity. The second significant parameter influencing thermal behavior is the feed gas relative humidity, as inlet humidification strongly affects the degree of overall membrane hydration. It is seen from Eqs. (20)–(22) that the proton conductivity of the membrane is directly proportional to water activity, indicating the more important role of the temperature distribution in low-humidity operation. In contrast, the thermal effect becomes less dramatic when the inlet gases are fully humidified because the membrane most likely remains fully hydrated. The last critical parameter is the operating cell voltage as it controls the current output and thus the heat generation rate.

The model input parameters and physical properties used in the parametric study described above are listed in Table 2, including the geometrical dimensions and properties of MEA. The thermal conductivities for various sub-layers and gases in a fuel cell are presented in Table 3. For all cases, the anode and cathode inlet pressures are fixed at 3.18 atm. In addition, anode and cathode stoichiometries of 1.2 and 2.0 based on the reference current density of 1.5 A/cm^2 are employed. The cell temperature, applied to the inlet gases as well as the surface
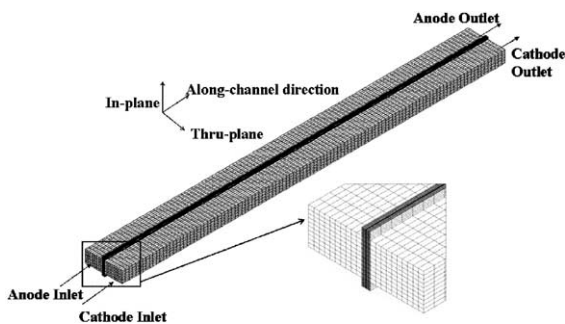
Table 3
Thermal properties

Material	Thermal conductivity [W/m K]
Hydrogen (H_2), k_{H_2}	0.2040
Oxygen(O_2), k_{O_2}	0.0296
Water vapor, k_w	0.0237
Nitrogen(N_2), k_{N_2}	0.0293
Membrane, k_{mem}	0.950
Gas diffusion layer, k_{GDL}	0.5, 1.0, 2.94

of current collector ribs, is set at 80 °C. The parametric study consists of three GDL thermal conductivity values (k_{GDL} = 0.5, 1.0, and 2.94 W/m K), two operating cell voltages (V_{cell} = 0.7 and 0.6 V), and two inlet humidity conditions (RH_a/RH_c = 75%/0% and 100%/100%). So a total of twelve non-isothermal simulations are carried out along with four corresponding isothermal cases for comparison. The average current densities and membrane temperatures computed for these sixteen cases are summarized in Table 4. To facilitate the following discussions, various parametric cases are labeled by a combination of letter "L" (low-humidity with RH_a/RH_c = 75%/0%) or "F" (fully humidified), an integral number "7" (for the cell voltage of 0.7 V) or "6" (for 0.6 V), followed by letters "a", "b", "c", and "d" corresponding to the isothermal baseline case, k_{GDL} = 0.5, 1.0, and 2.94 W/m K, respectively. That is, a case denoted by "L7a" means the low humidity and isothermal conditions at the cell voltage of 0.7 V.

It is seen from Table 4 that the higher cell voltage case produces the lower current density and hence lower membrane temperature rise, as expected. Also notice that the average membrane temperature is strongly influenced by the GDL thermal conductivity, indicating a significant role played by lateral heat conduction

through the GDL in the removal of waste heat to the ambient. Additionally, we have estimated the amount of heat transferred by gas convection and the wall-to-wall radiation through the gas channel, and found that the gas convection and radiation remove no greater than 1% and 2% of the total heat, respectively.

For the fully humidified cases, Table 4 shows that the average current density increases with decreasing GDL thermal conductivity and hence increasing membrane temperature. This indicates that the thermal effect on ORR kinetics dominates the possible membrane dehydration, thus leading to an improved overall performance. One exception is case F6d where the average membrane temperature increases by about 13.5 °C, sufficiently substantial to cause severe membrane dehydration and hence lower the overall current density. Such a large temperature variation is likely encountered under higher operating temperatures and higher power densities, an important direction that the automotive industry is moving towards.

Table 4 also shows that, for the low-humidity cases at 0.6 V (L6a–L6d), the performance significantly decreases with increasing membrane temperature, indicating that the membrane hydration effect is more dominant. As k_{GDL} is equal to 0.5 W/m K (L6d), the performance is roughly 20% lower than the isothermal case (L6a), which corresponds to an infinitely large thermal conductivity. Therefore, a GDL material having higher thermal conductivity is strongly recommended for fuel cells designed to operate under low-humidity (e.g. L6a–L6d). However the same trend clearly does not exist in the low humidity cases at 0.7 V (i.e. L7a–L7d), implying that for all L7 cases the kinetic dependence on temperature dominates the membrane hydration effect. The low range of the current density around 0.35 A/cm² belongs to the kinetic control regime in a polarization curve.

Table 4
Parametric study results at T_{cell} = 353.15 K

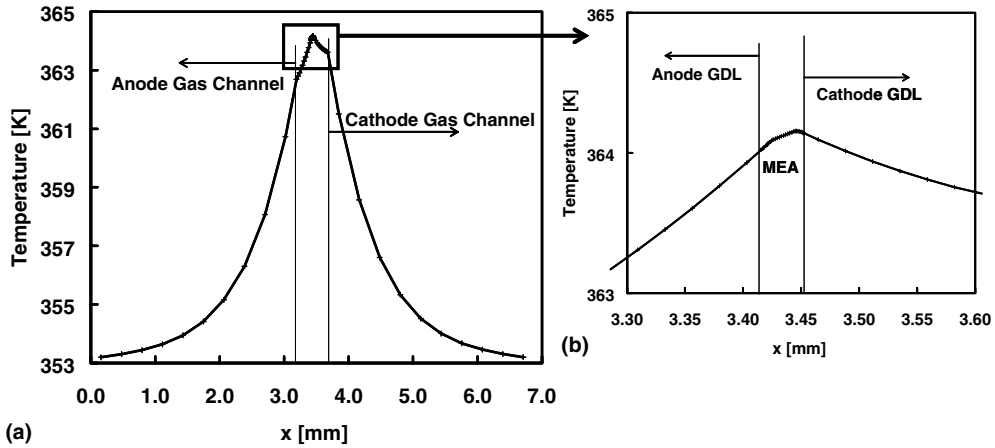|	V_{cell} = 0.7 V		V_{cell} = 0.6 V	
Low humidity inlet (RH_a/RH_c = 75%/0%)	L7a Isothermal model	I_{avg} = 3469 A/m²	L6a Isothermal model	I_{avg} = 9719 A/m²
	L7b k_{GDL} = 2.94 W/m K	I_{avg} = 3483 A/m² T_{avg} = 353.8 K	L6b k_{GDL} = 2.94 W/m K	I_{avg} = 9130 A/m² T_{avg} = 355.2 K
	L7c k_{GDL} = 1.0 W/m K	I_{avg} = 3519 A/m² T_{avg} = 354.9 K	L6c k_{GDL} = 1.0 W/m K	I_{avg} = 8389 A/m² T_{avg} = 357.7 K
	L7d k_{GDL} = 0.5 W/m K	I_{avg} = 3558 A/m² T_{avg} = 356.0 K	L6d k_{GDL} = 0.5 W/m K	I_{avg} = 7985 A/m² T_{avg} = 360.3 K
Fully humidified inlet (RH_a/RH_c = 100%/100%)	F7a Isothermal model	I_{avg} = 8179 A/m²	F6a Isothermal model	I_{avg} = 14530 A/m²
	F7b k_{GDL} = 2.94 W/m K	I_{avg} = 8369 A/m² T_{avg} = 354.9 K	F6b k_{GDL} = 2.94 W/m K	I_{avg} = 14837 A/m² T_{avg} = 356.7 K
	F7c k_{GDL} = 1.0 W/m K	I_{avg} = 8720 A/m² T_{avg} = 357.6 K	F6c k_{GDL} = 1.0 W/m K	I_{avg} = 15014 A/m² T_{avg} = 362.0 K
	F7d k_{GDL} = 0.5 W/m K	I_{avg} = 8796 A/s m² T_{avg} = 360.4 K	F6d k_{GDL} = 0.5 W/m K	I_{avg} = 14466 A/m² T_{avg} = 366.7 K

Fig. 2. Temperature profiles along the through-plane direction for Case L6d ($RH_a/RH_c = 75\%/0\%$, $V_{cell} = 0.6\,V$, $k_{GDL} = 0.5\,W/m\,K$).

Fig. 2a and b show the temperature profiles in the through-plane direction for case L6d. The temperature data were taken at the half-length of the cell cutting across the middle of the flow channel. The temperature peak appears in the cathode catalyst layer, implying that major heat generation takes place in the region.

The temperature distributions along the flow direction for Cases L6b–L6d are shown in Fig. 3, where the temperatures are cross-sectional averages in the through-plane and in-plane directions. In every case, the membrane temperature facing the gas channel (referred to "mc") is higher than that facing the ribs (referred to "mr") as the ribs are a heat sink. The aver-

age temperature in the cathode gas channel (referred to "cgc") is the lowest as the gas convection effect is weak. Fig. 4 displays the water activity distributions in the membrane along the flow direction for Cases L6a–L6d, including the isothermal baseline case, L6a. In all cases, the water activity increases toward the outlet as the dry membrane gains water from the continual water production by ORR. In addition, the water activities facing the ribs are higher than those facing the channels due partly to a lower local temperature near the ribs and partly to the fact that the ribs protect the membrane from losing water through the GDL. It is also seen that the lower water activity is predicted for the case of lower
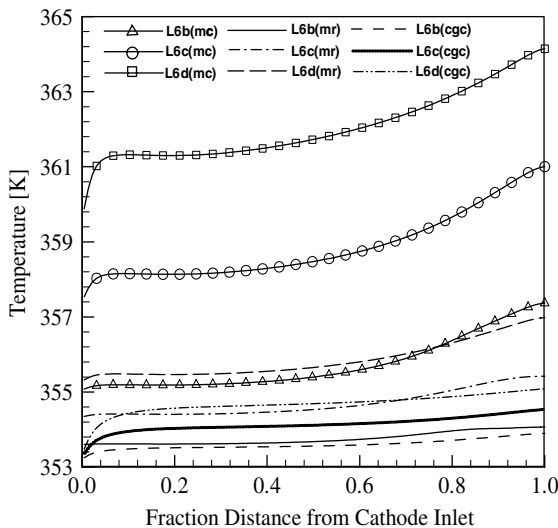

Fig. 3. Temperature distributions in different regions along the flow direction for L6b–L6d cases ($RH_a/RH_c = 75\%/0\%$, $V_{cell} = 0.6\,V$).
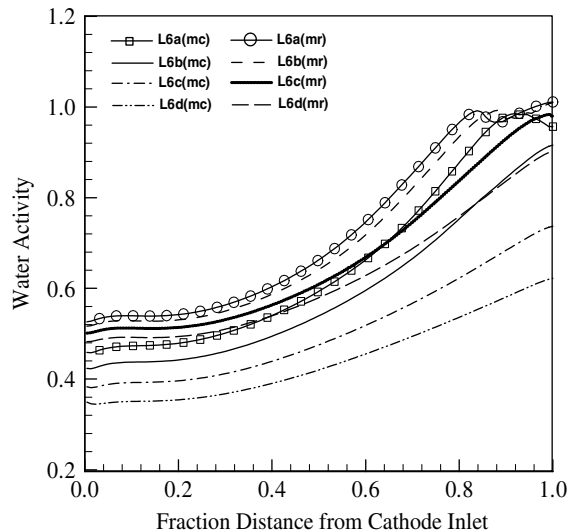

Fig. 4. Water activity distributions in different regions of the membrane along the flow direction for L6a–L6d cases ($RH_a/RH_c = 75\%/0\%$, $V_{cell} = 0.6\,V$).

GDL thermal conductivity and hence the larger membrane temperature rise. Fig. 4 also indicates the water activity is below unity in all cases under consideration, implying that the membrane is under-hydrated. The corresponding current density distributions are shown in Fig. 5. Since the membrane is under-humidified in all cases under consideration, as evident from the water activity always below unity in Fig. 4, the current density profile mirrors that of the water activity. It can thus be concluded that the current density distributions for all L6 cases are controlled by membrane hydration. As a consequence, it is seen in Fig. 5 that the local current density in the rib region is higher than in the channel due to the less drier membrane and thus better proton conductivity in the former. Also notice that the membrane temperature shown in Fig. 3 increases along the flow direction, following the current density profile shown in Fig. 5.

The temperature distributions for the fully humidified, 0.7 V cases are shown in Fig. 6. Again, higher temperatures are predicted in the membrane facing the gas channel and with the lower GDL thermal conductivity. Fig. 7 shows the water activity distributions along the flow direction. Under the fully humidified inlet conditions at 80 °C, the membrane water activities in Cases F7c and F7d facing the gas channel become even lower than unity until 30% and 70% into the gas channel, respectively, due to the significant membrane temperature rise. On the other hand, the membrane water activities in the rib region are all higher than unity due to lower local temperature. This result suggests that GDL

Fig. 6. Temperature distributions on different regions along the flow direction for F7b–F7d cases ($RH_a/RH_c = 100\%/100\%$, $V_{cell} = 0.7$ V).

Fig. 7. Water activity distributions in different regions of the membrane along the flow direction for F7a–F7d cases ($RH_a/RH_c = 100\%/100\%$, $V_{cell} = 0.7$ V).
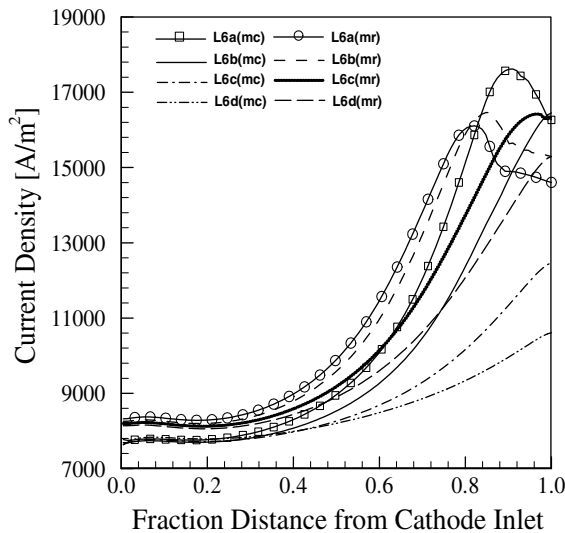

Fig. 5. Current density distributions in different regions of the membrane along the flow direction for L6a–L6d cases ($RH_a/RH_c = 75\%/0\%$, $V_{cell} = 0.6$ V).
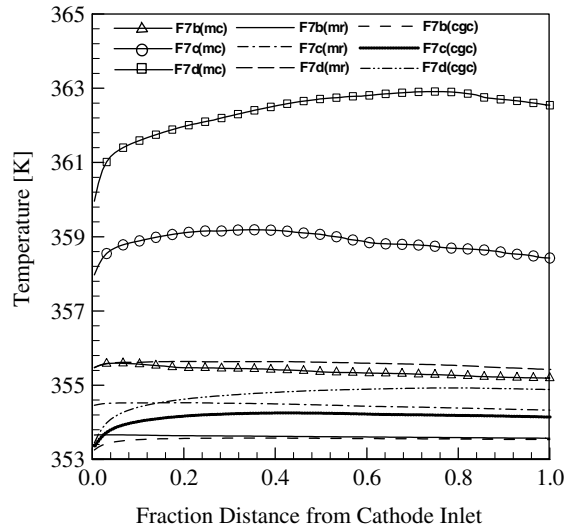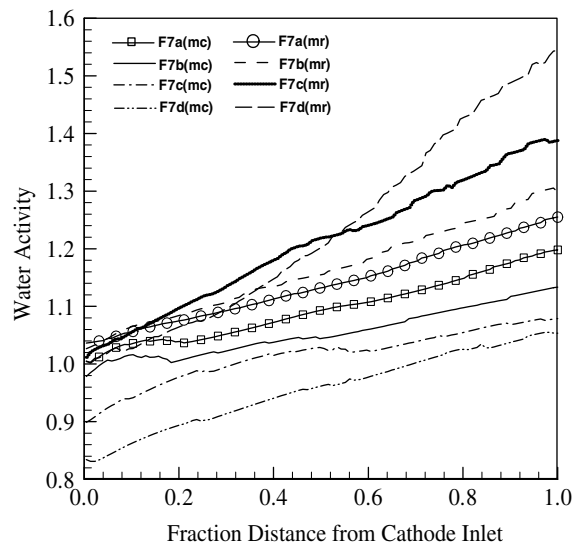
above the rib is more prone to flooding by liquid water. The current density distributions shown in Fig. 8 for the fully humidified inlet condition are vastly different from those of the low-humidity cases as shown in Fig. 5. First, the current densities in the gas channel region are higher than those in the rib region, indicating that the fuel cell performance is determined by the oxygen transport
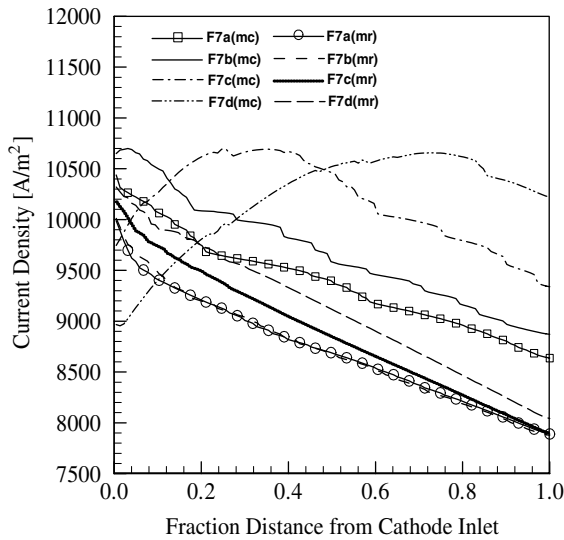
Fig. 8. Current density distributions in different regions of the membrane along the flow direction for F7a–F7d cases (RH$_a$/RH$_c$ = 100%/100%, V_{cell} = 0.7 V).

limitation under the fully humidified condition. In Cases F7a and F7b, the current density in both channel and rib regions decreases monotonically toward the downstream due to oxygen depletion. However, the current density distributions in Cases F7c and F7d cases, where heat transfer is less effective, exhibit a qualitatively different pattern. It shows a increase from the inlet to the middle portion of the fuel cell, and then a decrease towards the outlet. This pattern is developed because the local current density is controlled first by under-hydrated membrane and then by oxygen depletion once the membrane becomes fully hydrated towards the fuel cell outlet.

Fig. 9 plots the temperature contours in the mid-plane of the membrane for Cases L6b, L6d, F7b, and F7d. In accordance with other results, it is seen that the temperature rise in the membrane depends strongly on the GDL thermal conductivity and inlet humidification conditions. The maximum temperature rises in Cases L6b, L6d, F7b, and F7d are 5.45 °C, 13.75 °C, 3.25 °C, and 12.65 °C, respectively. There is roughly 8–9 °C difference in the maximum temperature rise between the GDL thermal conductivities of 2.94 and 0.5 W/m K.

Table 5 presents an analysis of overall heat balance as well as the various heat source terms for all cases of k_{GDL} = 1.0 W/m K. It is seen that the total sum of all heat sources computed from the 3D numerical model agrees reasonably well with the overall heat generation rate calculated from the simple equation, Eq. (3). These calculations demonstrate the validity and accuracy of
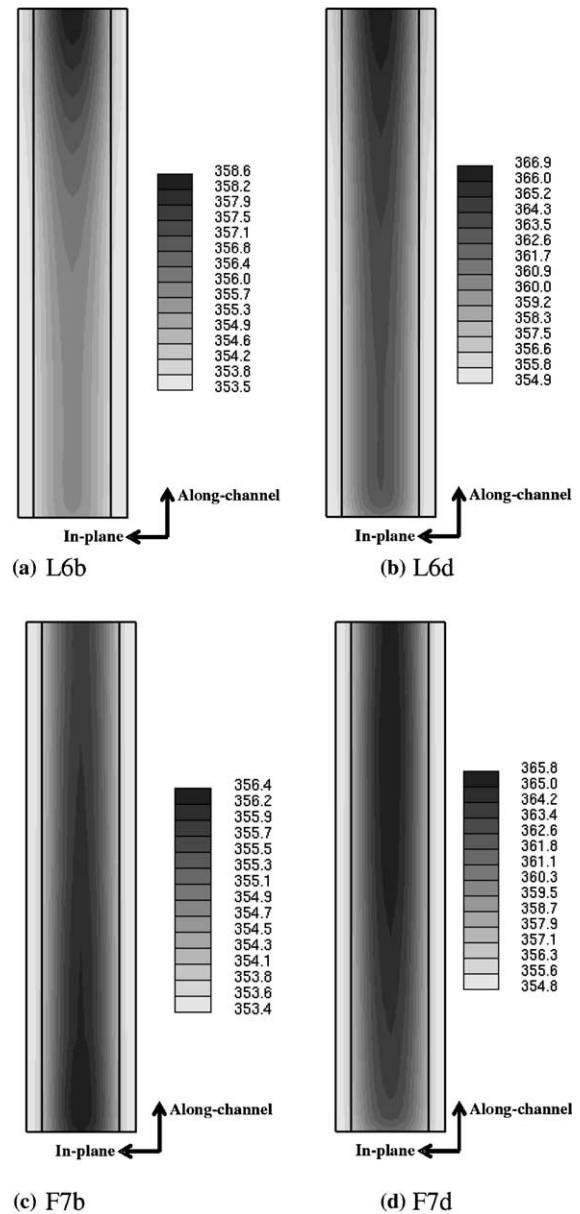

Fig. 9. Temperature contours over the middle of the membrane.

the present non-isothermal PEMFC model. The results further indicate that the most heat is released from the irreversible reaction and entropic heat sources in the cathode catalyst layer. In addition, the net energy efficiency of the fuel cell, η_e, is calculated and shown also in Table 5. The energy efficiencies for the cell voltages of 0.7 and 0.6 V are thus calculated to be ∼47% and 40%, respectively, regardless of the inlet humidity conditions.

Table 5
Summary of energy balance results

	$A_{react} = 2.17\,cm^2$	L7c	L6c	F7c	F6c
Total heat released	Eq. (3) [W]	0.6083	1.6319	1.5072	2.9206
(1) Anode catalyst layer	Irreversible reaction heat, [W]	0.0074	0.0404	0.0260	0.0999
	$S_{T,irrev,a} = \int_V j \cdot \eta\, dV$	(1.21%)	(2.45%)	(1.72%)	(3.40%)
	Ohmic joule heating, [W]	0.0052	0.0292	0.0177	0.0658
	$S_{T,jouleH,a} = \int_V \frac{I}{\kappa^{eff}}\, dV$	(0.85%)	(1.77%)	(1.17%)	(2.24%)
(2) Membrane	Ohmic joule heating, [W]	0.0544	0.2107	0.0645	0.2179
	$S_{T,jouleH,mem} = \int_V \frac{I}{\kappa^{eff}}\, dV$	(9.04%)	(12.75%)	(4.26%)	(7.41%)
(3) Cathode catalyst layer	Irreversible reaction heat, [W]	0.2865	0.7428	0.7748	1.4411
	$S_{T,irrev,c} = \int_V j \cdot \eta\, dV$	(46.69%)	(44.95%)	(51.21%)	(48.99%)
	Ohmic joule heating, [W]	0.0154	0.0442	0.0217	0.0559
	$S_{T,jouleH,c} = \int_V \frac{I}{\kappa^{eff}}\, dV$	(2.51%)	(2.67%)	(1.43%)	(1.90%)
	Entropic heat, [W]	0.2436	0.5850	0.6084	1.0612
	$S_{T,rev,c} = \int_V j \cdot (T \frac{\partial U_0}{\partial T})\, dV$	(39.71%)	(35.40%)	(40.21%)	(36.07%)
Sum	(1) + (2) + (3), [W]	0.6136	1.6523	1.5131	2.9418
Energy efficiency, η_e	Eq. (4)	0.47	0.40	0.47	0.40

4. Conclusions

A three-dimensional, non-isothermal PEMFC model has been developed by paying particular attention to the precise and location-specific forms of various heat sources generated from a PEM fuel cell. The main interest of this study was to assess the thermal effects on a PEM fuel cell under different design and operating conditions. A parametric study was performed for three critical parameters: the GDL thermal conductivity, the feed gas relative humidity, and the operating cell voltage.

The results show that the GDL thermal conductivity strongly impacts the membrane temperature rise, and thus plays an important role in coupled thermal and water management of PEM fuel cells. There exist vastly different thermal behaviors under different humidification conditions. In the medium range of current density (i.e. the ohmic control regime of *IV* curve), the low inlet humidity cases (L6) show a significant decrease in fuel cell performance as the membrane temperature rises, indicating that the fuel cell performance is primarily controlled by membrane hydration. Thus, efficient cooling through the current collector ribs becomes critical in low-humidity operation in order to maintain good membrane proton conductivity. On the other hand, for fully humidified cases, the performance is dominated by ORR kinetics and therefore becomes higher with larger membrane temperature rises. In addition, severe flooding of electrodes is more likely in the fully humidified operation, particularly in the cold region near ribs. Therefore relatively higher membrane temperature rise enabled by low GDL thermal conductivity should be helpful to alleviate electrode flooding and enhance the ORR kinetics.

The energy balance analysis presented in Table 5 compared the numerically computed heat sources with the thermodynamic calculation of the overall heat generation with good agreement. This exercise, carried out for the first time in the literature, is useful to verify the appropriateness of heat source terms used in a PEMFC thermal model. Further, it was revealed that the irreversible reaction heat and entropic heat in the cathode catalyst layer are the major contributors to heat generation in PEM fuel cells, accounting for roughly 80 to 90% of the total waste heat released.

The present study also indicates that the thermal effects strongly affect the current density distribution, demonstrating a necessity for non-isothermal modeling of PEM fuel cells. Work is underway to validate the present non-isothermal model against the experimental data of not only the current distribution but also the membrane temperature distribution measured in situ in an operating PEM fuel cell. In addition, the present non-isothermal model is being integrated into a two-phase model where water condensation/evaporation process provides another strong link between water and heat management in PEM fuel cells.

References

[1] J. Newman, Electrochemical Systems, Prentice-Hall, Englewood Cliffs, NJ, 1991, pp. 290–291.

[2] T.V. Nguyen, R.E. White, A water and heat management model PEMFCs, J. Electrochem. Soc. 140 (1993) 2178–2186.

[3] T.F. Fuller, J. Newman, Water and thermal management in solid-polymer-electrolyte fuel cells, J. Electrochem. Soc. 140 (1993) 1218–1225.

[4] J.S. Yi, T.V. Nguyen, An along-the-channel model for proton exchange membrane fuel cells, J. Electrochem. Soc. 145 (1998) 1149–1159.

[5] M. Wöhr, K. Bolwin, W. Schnurnberger, M. Fischer, W. Neubrand, Dynamic modeling and simulation of a polymer membrane fuel cell including mass transport limitation, Int. J. Hydrogen Energy 23 (1998) 213–218.

[6] A. Rowe, X. Li, Mathematical modeling of PEMFCs, J. Power Sour. 102 (2001) 82–96.

[7] G. Maggio, V. Recupero, C. Mantegazza, Modeling of temperature distribution in a solid polymer electrolyte fuel cell stack, J. Power Sour. 62 (1996) 167–174.

[8] S. Shimpalee, S. Dutta, Numerical prediction of temperature distribution in PEM fuel cells, Num. Heat Transfer Part A 38 (2000) 111–128.

[9] P. Costamagna, Transport phenomena in polymeric membrane fuel cells, Chem. Eng. Sci. 56 (2001) 323–332.

[10] T. Berning, D.M. Lu, N. Djilali, 3-D computational analysis of transport phenomena in a PEM fuel cell, J. Power Sour. 106 (2002) 284–294.

[11] T. Zhou, H. Liu, A general three-dimensional model for proton exchange membrane fuel cell, Int. J. Trans. Phenom. 3 (2001) 177–198.

[12] C. Berger, Handbook of Fuel Cell Technology, Prentice-Hall, NJ, 1968.

[13] S. Um, C.Y. Wang, K.S. Chen, Computational fluid dynamics modeling of proton exchange membrane fuel cells, J. Electrochem. Soc. 147 (2004) 4485–4493.

[14] W.B. Gu, C.Y. Wang, Thermal–electrochemical modeling of battery systems, J. Electrochem. Soc. 147 (2000) 2910–2922.

[15] T.E. Springer, T.A. Zawodinski, S. Gottesfeld, Polymer electrolyte fuel cell model, J. Electrochem. Soc. 136 (1991) 2334–2341.

[16] R.E. Meredith, C.W. Tobias, Conduction in heterogeneous systems, in: C.W. Tobias (Ed.), Advances in Electrochemistry and Electrochemical Engineering, Interscience Publishers, New York, 1962.

[17] D.M. Bernardi, M.W. Verbrugge, Mathematical model of a gas diffusion electrode bonded to a polymer electrolyte, AIChE J. 37 (1991) 1151–1163.

[18] S. Gottesfeld, T.A. Zawodzinski, Polymer electrolyte fuel cells, in: C. Tobias (Ed.), Advances in Electrochemical Science and Engineering, vol. 5, John Wiley & Sons, New York, 1997, pp. 195–301.

[19] A. Parthasarathy, S. Srinivasan, A.J. Appleby, Temperature dependence of the electrode kinetics of oxygen reduction at the platinum/nafion® interface—a microelectrode investigation, J. Electrochem. Soc. 139 (1992) 2530–2537.

[20] R.B. Bird, W.E. Stewart, E.N. Lightfoot, Transport phenomena, John Wiley & Sons, New York, 1960.

[21] S. Motupally, A.J. Becker, J.W. Weidner, Diffusion of water in nafion 115 membranes, J. Electrochem. Soc. 147 (2000) 3171–3177.

[22] STAR-CD Version 3.15 methodology, CD-Adapco Group, 2001.

[23] H. Meng, C.Y. Wang, Large-scale simulation of polymer electrolyte fuel cells by parallel computing, Chem. Eng. Sci. 59 (2004) 3331–3343.